catalysts

MDPI

Article

The Influence of Au Loading and TiO_2 Support on the Catalytic Wet Air Oxidation of Glyphosate over TiO_2+Au Catalysts

Gregor Žerjav [1,*], Alen Albreht [2] and Albin Pintar [1]

[1] Department of Inorganic Chemistry and Technology, Laboratory for Environmental Sciences and Engineering, National Institute of Chemistry, Hajdrihova 19, SI-1001 Ljubljana, Slovenia; albin.pintar@ki.si
[2] Department of Analytical Chemistry, Laboratory for Food Chemistry, National Institute of Chemistry, Hajdrihova 19, SI-1001 Ljubljana, Slovenia; alen.albreht@ki.si
* Correspondence: gregor.zerjav@ki.si

Abstract: This study aimed to explore the impact of varying amounts of added Au (0.5 to 2 wt.%) and the structural characteristics of anatase TiO_2 supports (nanoparticles (TP, S_{BET} = 88m^2/g) and nanorods (TR, S_{BET} = 105 m^2/g)) on the catalytic efficiency of TiO_2+Au catalysts in eliminating the herbicide glyphosate from aqueous solutions via the catalytic wet air oxidation (CWAO) process. The investigation was conducted using a continuous-flow trickle-bed reactor. Regardless of the TiO_2 support and the amount of Au added, the addition of Au has a positive effect on the glyphosate degradation rate. Regarding the amount of Au added, the highest catalytic activity was observed with the TP + 1% Au catalyst, which had a higher Schottky barrier (SB) than the TP + 2% Au catalyst, which helped the charge carriers in the TiO_2 conduction band to increase their reduction potential by preventing them from returning to the Au. The role of glyphosate degradation product adsorption on the catalyst surface is crucial for sustaining the long-term catalytic activity of the investigated TiO_2+Au materials. This was particularly evident in the case of the TR + 1% Au catalyst, which had the highest glyphosate degradation rate at the beginning of the CWAO experiment, but its catalytic activity then decreased over time due to the adsorption of glyphosate degradation products, which was favoured by the presence of strong acidic sites. In addition, the TR + 1% Au solid had the smallest average Au particle size of all analyzed materials, which were more easily deactivated by the adsorption of glyphosate degradation products. The analysis of the degradation products of glyphosate shows that the oxidation of glyphosate in the liquid phase involves the rupture of C–P and C–N bonds, as amino-methyl-phosphonic acid (AMPA), glyoxylic acid and sarcosine were detected.

Keywords: glyphosate; catalytic wet air oxidation; noble metals; gold nanoparticles; trickle-bed reactor; water treatment

Citation: Žerjav, G.; Albreht, A.; Pintar, A. The Influence of Au Loading and TiO_2 Support on the Catalytic Wet Air Oxidation of Glyphosate over TiO_2+Au Catalysts. *Catalysts* **2024**, *14*, 448. https://doi.org/10.3390/catal14070448

Academic Editor: Juan García Rodríguez

Received: 11 June 2024
Revised: 8 July 2024
Accepted: 10 July 2024
Published: 12 July 2024

1. Introduction

The utilization of the wet air oxidation (WAO) process is highly appealing for treating wastewater that is either too toxic for biological purification or too diluted for incineration [1]. The use of WAO in large-scale wastewater treatment is limited due to energy demanding processes (high temperature and high pressure), which cause high operating costs. The addition of a suitable catalyst mitigates the WAO process by increasing the reaction rate, shortening the reaction time, and reducing the operating costs [2,3]. In the catalytic WAO (CWAO) process, organic impurities are oxidised to form biodegradable intermediates or mineralised to water, CO_2, and corresponding inorganic salts, facilitated by activated O_2 species in the presence of catalysts. This takes place in a temperature range of 130 to 250 °C and at a pressure of 10 to 50 bar [4]. Mixed metal oxide systems, metal oxides, noble metal catalysts supported on materials like titanium oxide (TiO_2) and

cerium-based composite oxides have been studied for catalytic wet air oxidation (CWAO) of diverse organic pollutants [4–8].

The widely used broad-spectrum herbicide glyphosate (*N*-(phosphonomethyl)glycine) is potentially carcinogenic and can cause endocrine disruption in humans even at trace levels (<0.02 mg/L) [9–12]. In Europe, glyphosate accounts for a third of all herbicides used. The discussion concerning a possible ban on the use of glyphosate was triggered by concerns about its possible indirect and direct effects on the environment and human health. Several European countries have announced that they will ban or severely restrict the use of glyphosate in the future [13–16]. The U.S. Environmental Protection Agency has set the permitted level for glyphosate in water at 700 μg/L [17], while EU regulations have set this level at 0.1 μg/L [18,19]. Complete mineralization of glyphosate by conventional wastewater treatment processes is difficult due to the high chemical stability of the glyphosate molecule, which is due to the presence of C–N and C–P bonds [20,21]. The widespread use of glyphosate, improper handling of herbicide-containing containers, and its good solubility in water (11.6 g/L, 25 °C) led to an increase in herbicide concentrations in groundwater or surface water, resulting in reported glyphosate concentrations of up to 76 mg/L [22–24]. Gupt et al. [25] studied the mineralization of glyphosate in CWAO using carbon nanofibers (CNF) with iron nanoparticles (Fe NP) deposited on activated carbon beads (ACB) as a catalyst (0.75 g/L catalyst dose) with high thermal stability (25–1100 °C) and high S_{BET} value (~296 m^2/g). After 2 h at 220 °C and 25 bar atmospheric pressure, ~70% degradation of aqueous glyphosate (100 mg/L) was achieved. Complete degradation of glyphosate was achieved after 6 h under the same experimental conditions when Fe-CNF/ACB with higher specific surface area (~338 m^2/g), Fe loading of 4 mg/g, increased exposure of Fe-NPs to the surrounding liquid, and graphitic properties (ID/IG = 0.946) of CNFs were used [26]. Xing et al. [27]carried out CWAO of water-dissolved glyphosate (500–2500 mg/L) at 10 bar and 130 °C using activated carbons modified by H_2O_2 oxidation and thermal treatment with ammonia or melamine as catalysts and obtained ~97% removal of glyphosate in the continuous 55-day test.

The objective of this study was to thoroughly examine how varying amounts of added Au and the structural characteristics of anatase TiO_2 supports (nanoparticles (TP) and nanorods (TR)) influence the catalytic performance of TiO_2+Au catalysts in the degradation of the water-dissolved herbicide glyphosate. This investigation was conducted using a continuous-flow trickle-bed reactor operating under low-interaction conditions (scheme of the reactor system in [28]). Liquid chromatography and UV spectrophotometry coupled with mass spectrometry were employed to explore and quantify potential transformation products of glyphosate, aiming to identify predominant by-products and elucidate a plausible oxidation pathway of glyphosate via the CWAO process. To our knowledge, this is the first application of TiO_2+Au catalysts for the CWAO of glyphosate dissolved in water.

2. Results and Discussion

2.1. Catalyst Characterization

The XRD diffraction patterns of the investigated solids illustrated in Figure 1 show the main diffraction peaks of anatase TiO_2 in all cases. No diffraction peaks were detected that would belong to other TiO_2 polymorphs. For the Ti_2O+Au catalysts, no diffraction peaks belonging to gold were observed, which could be due to several facts such as: (i) low gold loading, (ii) presence of small gold particles, (iii) good distribution of gold on the surface of the TiO_2 supports, etc. [29–32]. The Scherrer equation, utilizing the main diffraction peak of anatase at $2\theta = 25.3°$, was used to determine the average anatase crystallite sizes, which are shown in Table 1. We can see that there is a difference between the average anatase crystallite sizes of the bare TiO_2 supports of about 5 nm and that the TP sample has the highest anatase crystallite size of 21.3 nm. Furthermore, we can

conclude that the wet impregnation process used had no influence on the average anatase crystallite size, regardless of which TiO_2 support was used.

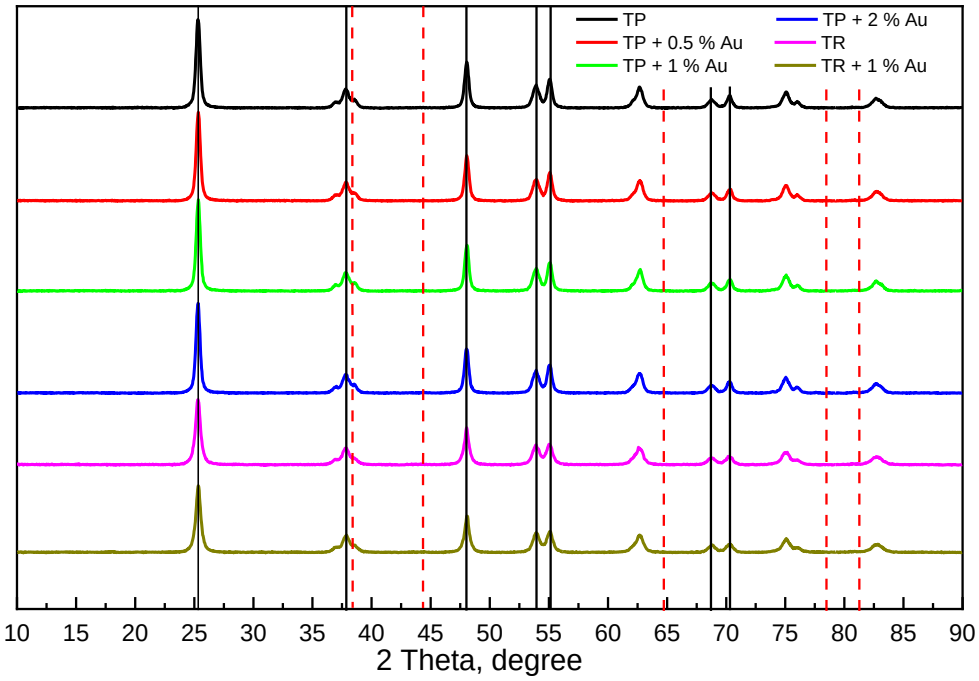

Figure 1. XRD patterns of both pure TiO_2 supports and TiO_2+Au catalysts with varying Au loadings are presented. In these patterns, solid vertical lines indicate anatase TiO_2 (JCPDS 00-021-1272), while dotted vertical lines denote fcc Au (JCPDS 01-1174).

The SEM images, N_2 adsorption–desorption isotherms and the corresponding BJH pore size distributions of the investigated solids are shown in Figures 2 and S2. Table 1 shows the results of the N_2 adsorption–desorption measurements (S_{BET}, V_{pore} and d_{pore}). The obtained SEM and TEM images of the TiO_2+Au catalysts reveal that there is a difference in the morphology of the synthesized catalysts depending on which TiO_2 support was used. In the case of the TP sample, we can observe elongated TiO_2 particles with a length of 40 nm and a diameter of about 30 nm, while in the case of the TR solid as the TiO_2 support, we can clearly observe TiO_2 in the form of nanorods with a length of 80–100 and a diameter of about 20 nm. The results of the N_2 adsorption–desorption measurements performed on the investigated materials (Table 1 and Figure S1) reflect well the differences in the TiO_2 support shapes, where the TR-based materials (S_{BET}(TR+Au) = 94–105 m^2/g) have a higher specific surface area (of about 20%) compared to the TP-based materials (S_{BET}(TP+Au) = 71–88 m^2/g). The results also show that impregnating TiO_2 supports with gold did not significantly affect the average pore diameter and the total pore volume compared to the pure TiO_2 supports. This fact indicates that the gold particles were mainly distributed over the surface of the TiO_2 supports and not incorporated into the TiO_2 supports [33]. Scanning electron microscopy was also used to obtain data on the actual gold loading in the fabricated TiO_2+Au catalysts compared to the nominal gold loading. The results of the SEM–EDS analysis can be found in Table S1, which shows that the actual gold loading is almost equal to the nominal for all TiO_2+Au catalysts investigated. The SEM–EDS elemental mapping images of the investigated TiO_2+Au catalysts in Figure S2 also show a good distribution of gold in the synthesized TiO_2+Au catalysts. The diagrams of the gold particle size distribution illustrated in Figure S4 were prepared using transmission electron microscopy (Figure S3). The results in Figure S4 and Table 1 show that the size distribution of the gold particles and the average gold particle size depend on the used TiO_2 substrate (d_{Au}(TR+Au) = 9.2 nm and d_{Au}(TP+Au) = 37–54 nm). The TR+Au catalysts show a narrow size distribution of Au particles

compared to the TP+Au catalysts, where a broader size distribution of Au particles is observed. This could be due to the fact that the TiO_2 supports have different BET specific surface areas and a different shape of the curve representing the dependence of the zeta potential on the pH of the solution, as shown in Figure S5. The pH value of the $HAuCl_4 \times 3H_2O$ aqueous solution used to prepare TiO_2+Au catalysts with 1 wt.% gold content was 3.4. In Figure S5, we can see that, at this pH value, the surfaces of the TiO_2 supports were positively charged, which promoted the adsorption of $(Au(OH)_3Cl)^-$ by an electrostatic effect that was stronger in the case of the TP support (20 mV) than in the case of the TR support (10 mV). For the TP+Au catalysts, we can observe that, by adding more $HAuCl_4 \times 3H_2O$ to the aqueous solution to obtain catalysts with a higher Au content, the pH value of the $HAuCl_4 \times 3H_2O$ solution also decreased. This led to an increase in the surface charge of the TP support, which had an additional positive effect on the formation of larger gold clusters in the TP + 2% Au catalyst, apart from the fact that, with the addition of more $HAuCl_4 \times 3H_2O$ to the solution, the so-called "clustering" effect also occurs, as has already been observed by other authors [34].

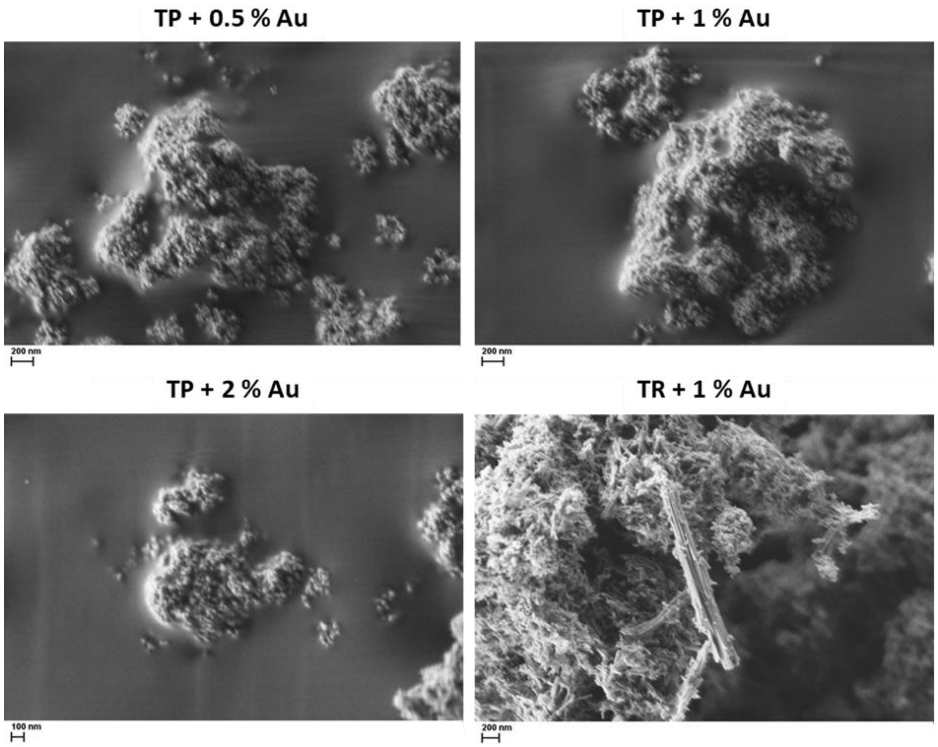

Figure 2. SEM images of the TiO_2+Au catalysts investigated.

Table 1. Comparison of specific surface area (S_{BET}), total pore volume (V_{pore}), average pore diameter (d_{pore}), Au particle size, anatase TiO_2 crystallite size, TiO_2 support diameter (d_{TiO_2}) and length (l_{TiO_2}), and Schottky barrier height (SBH) in the examined solids.

Sample	S_{BET}	V_{pore}	d_{pore}	d_{Au} *	Crystallite Size	d_{TiO_2}	l_{TiO_2}	SBH **
	m^2/g	cm^3/g	nm	nm	nm	nm	nm	eV
TP	88	0.30	14.8	/	21.3	30	40	/
TP + 0.5% Au	71	0.28	14.6	37.0	21.3			0.26
TP + 1% Au	74	0.29	14.2	36.9	21.3			0.22
TP + 2% Au	75	0.27	13.7	54.0	21.3			0.15
TR	105	0.57	19.3	/	16.7	20	80–100	/
TR + 1% Au	94	0.44	18.9	9.2	16.5			0.16

* Au particle size was calculated by counting more than 100 particles from acquired TEM images. ** Calculated from the determined values of VBM in Figure 3.

Figure S6 illustrates the UV–Vis DR spectra of the bare TiO_2 supports and the prepared TiO_2+Au. Across all materials, the UV–Vis DR spectra exhibit pronounced absorption in the wavelength range below 400 nm, attributable to the band gap of the TiO_2 supports [35]. The incorporation of Au resulted in heightened light absorption within the range of 450 to 600 nm. This enhancement can be ascribed to the existence of metallic Au nanoparticles within the TiO_2+Au catalysts and the consequent localized surface plasmon resonance effect induced by the plasmonic characteristics of Au [36,37]. A slight shift of the absorption edge in the UV light region of the TiO_2+Au catalysts compared to bare TiO_2 supports indicates that Au particles are deposited only on the surface of the TiO_2 supports [38], which is in agreement with the results of N_2 physisorption measurements. The outcomes of the solid-state PL measurements (depicted in Figure S7) show that all TiO_2+Au catalysts have lower solid-state PL intensities than the pure TiO_2 supports, which means that the catalysts have a lower charge carrier recombination rate than bare TiO_2. The lower charge carrier recombination rates in the TiO_2+Au catalysts indicate that there is a junction between the TiO_2 supports and the Au particles. At the interface between TiO_2 and Au, a barrier forms, i.e., the Schottky barrier (SB), which is an obstacle for the charge carriers when they want to migrate either from Au to TiO_2 or vice versa. Furthermore, the results of the PL measurements confirm the results of the XRD analysis, namely that the TiO_2 is present in the anatase form, as a characteristic anatase TiO_2 peak occurs at 3.17 eV [39,40]. In the solid state TiO_2+Au PL spectra a blue shift of the 3.17 eV peak to about 3.2 eV can be observed, as the gold particles suppress indirect phonon-assisted transitions in the anatase TiO_2 [41,42]. The peak at 2.9 eV indicates the lowest indirect transition Γ1b → X1a. The peaks at 2.7, 2.55 and 2.34 eV can be attributed to the existence of TiO_2 defects, oxygen vacancies and shallow trap levels [43,44].

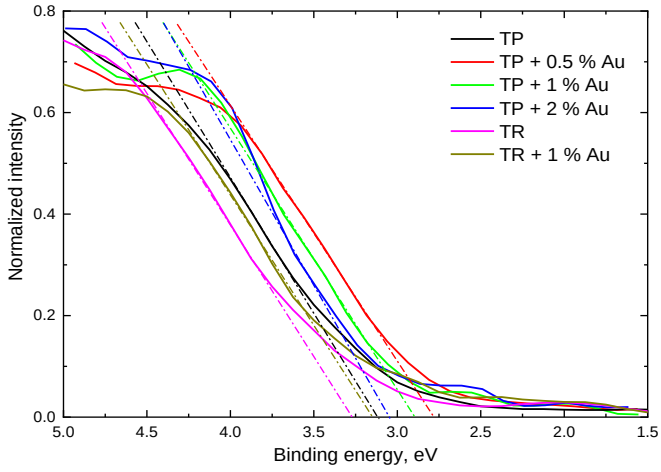

Figure 3. Determination of VBM of bare TiO_2 supports and TiO_2+Au catalysts by XPS analysis.

The high-resolution XPS spectra for O 1s, Ti 2p, and Au 4f of the analyzed materials are presented in Figure S8a–c. The O 1s binding energies for all analyzed materials are approximately 530.5 eV, corresponding to bulk oxide (O^{2-}) in the TiO_2 lattice (Figure S8a). In the high-resolution O 1s spectra of TP+Au catalysts, a high-energy shoulder appears about 0.9–1.5 eV above the main O^{2-} peak, attributed to weakly adsorbed species [45] or low-coordinated oxygen ions (O^-) indicating oxygen vacancies [46,47]. Figure S8 shows that the intensity of this high-energy shoulder (~532.4 eV) increases with the amount of Au in the TP+Au catalysts, suggesting an increase in oxygen vacancies and adhesion between Au and TiO_2. These oxygen vacancies can act as electrostatic field centres at the TiO_2–Au interface, enhancing the adhesion between Au and TiO_2 and forming a network of Au-O-Ti [48]. In the Ti 2p spectra of all materials (Figure S8), two peaks at ~464.9 eV (Ti $2p_{1/2}$) and ~459.2 eV (Ti $2p_{3/2}$) are observed, typical for Ti in the +4 oxidation state [49]. These results indicate that the chemical bonding between Ti and O remains consistent

across all materials studied, as the Ti $2p_{3/2}$ binding energy is ~459.2 eV in all samples (Figure S8b). The Au 4f spectra for the investigated TiO_2+Au catalysts are shown in Figure S8c. The Au $4f_{7/2}$ and Au $4f_{5/2}$ binding energies at 83.9 and 87.6 eV, respectively, match the reported values for fully reduced Au [50]. As already noted by other researchers [51], the intensity of the Au 4f peak increases with higher Au content in the TP+Au catalysts. The presence of a peak at 86.6 eV in the spectrum of the TNR + 1% Au catalyst suggests that amorphous Au_2O_3 (Au $4f_{7/2}$ = 86.9 eV) or other Au^{3+}-containing species (e.g., $Au(OH)_3$) could coexist with metallic Au on the surface of the TNR nanorods [52]. Figure 3 shows the results of the measurement of the valence band maxima (VBM) of the analyzed solids. The differences between the VBMs of the TiO_2 supports and the TiO_2+Au catalysts represent the height of the SBs [53] (Table 2). It is noticeable that, for TP-based solids, the Schottky barrier height decreases with the augmentation of Au content in the catalysts. Furthermore, the catalyst TR + 1% Au has a lower height of SB than the catalyst TP + 1% Au. For the charge carriers formed in Au, a high SB is not preferred as they need more time and energy to move to TiO_2, which causes them to bunch and recombine at SB. For the charge carriers moving from the TiO_2 conduction band to Au, a high SB is positive as they cannot move to Au and remain in the conduction band of TiO_2. This allows them to achieve higher energy levels, thereby increasing the reduction potential [54].

Besides the specific surface area, the separation of charge carriers, and the degree of crystallinity, the surface acidity of the investigated catalysts also significantly influences their behavior in the CWAO process [28,55]. To measure the surface acidic properties of the investigated catalysts, the temperature-programmed desorption (TPD) method was used with pyridine as the probe molecule (Figure 4). The temperatures at which the peaks of pyridine desorption appear during the TPD measurements, the density of the acidic sites and the number of acidic sites present in the studied solids are presented in Table 2. The positions of the peaks of pyridine desorption in high- or low-temperature ranges are due to the desorption of pyridine from strong or weak acidic sites. The presence of strong acidic sites on the catalyst surface could trigger either electrostatic interactions or side reactions, which in turn could lead to the accumulation of carbonaceous deposits on the catalyst surface (e.g., coking) and ultimately to the deactivation of the catalyst [28,56]. For the catalysts studied, it can be said that there is a linear trend between the decreasing number of acidic sites (from 0.210 mmol/g for the TR to 0.190 mmol/g for the TR + 1% Au) and the decreasing BET specific surface area of the solids studied (from 105 m^2/g for the TR to 94 m^2/g for the TR + 1% Au). For the two TiO_2+Au series produced, we can observe that, compared to the pure TiO_2 supports, the number of acidic sites decreases with the addition of gold and that, for the TP+Au series, the amount of acidic surface sites decreases drastically when the gold loading increases from 1 (0.139 mmol/g) to 2 wt.% (0.068 mmol/g). The distribution of the strength of the acidic sites, expressed by the temperatures of the peaks of pyridine desorption (Table 2 and Figure 4), shows that bare TP and TR supports exhibit the presence of medium and strong acidic sites, although the ratio between them is different. In the case of the TP sample, more strong acidic sites are present than weak acidic sites, while for the TR sample the trend is just the opposite. In addition, we must emphasize that we have also observed the desorption of pyridine from the TP sample in the temperature range above 700 °C (Figure 4). For the TR + 1% Au catalyst, it can be observed that the addition of gold did not alter the ratio of weak to strong acidic sites in comparison to the pure TR support. However, desorption of pyridine is still evident within the temperature range exceeding 750 °C. For the TP+Au series, the peak for the strong acidic site was shifted to lower temperatures in comparison to the bare TP support (from 550 °C for TP sample to 450 °C for TP + 0.5% Au and TP + 1% Au catalysts). In contrast, the TP + 2% Au sample showed a completely different distribution of the strength of the acidic sites than the pure TP support and the catalysts with 0.5 and 1 wt.% Au loadings. This could be due to the fact that the TP + 2% Au catalyst also showed the highest average gold particle size among all TP+Au catalysts investigated. It is evident that the presence of small gold nanoparticles in the TiO_2+Au catalysts has no effect on the

characteristics of the acidic-basic properties compared to bare TiO_2 supports, in contrast to larger gold nanoparticles, which is due to the change in metal–support interaction. Furthermore, in the case of the TP + 2% Au catalyst, we observed the desorption of pyridine in the temperature range above 700 °C, indicating the presence of strong acidic sites. This could lead to a decrease in the catalytic activity of the TP + 2% Au catalyst during the CWAO reaction, as the presence of strong acidic sites favours the accumulation of carbonaceous deposits [28]. We also performed the TPD analysis for the pure TiO_2 supports and the catalysts with 1 wt.% Au loading, which were calcined at 150 °C for 3 h prior to the measurements to simulate the effects of reaction temperature on the catalyst properties studied (Figure S9). The analysis reveals that calcination has no discernible impact on the quantity, density, or strength of the acidic sites in the investigated materials. This suggests that the properties of the studied catalysts remain unaffected by the operating conditions of the CWAO process.

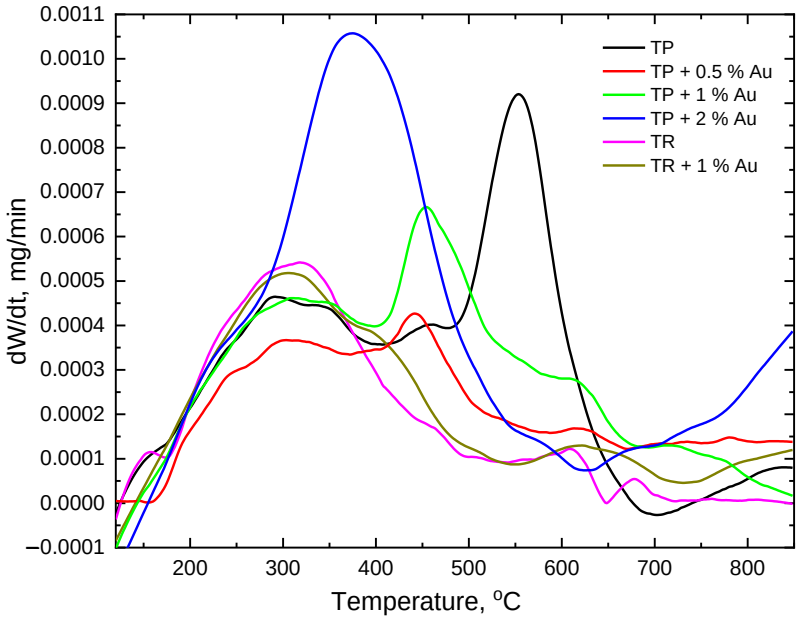

Figure 4. TPD of pyridine from the surface of the catalysts studied.

Table 2. Amount and density of acidic sites determined with TPD of pyridine for the catalysts studied.

Sample	Amount of Acidic Sites	Density of Acidic Sites	Peak of Pyridine Desorption
	mmol/g	mmol/(m²/g)	°C
TP	0.174	0.0019	312, 454, 554, above 700
TP *	0.183	0.0021	310, 450, 550
TP + 0.5% Au	0.121	0.0017	320, 441, 619
TP + 1% Au	0.139	0.0018	320, 453, 614
TP + 1% Au *	0.140	0.0018	318, 451, 613
TP + 2% Au	0.068	0.0009	376, above 700
TR	0.210	0.0020	310, 630
TR *	0.204	0.0019	310, 630
TR + 1% Au	0.190	0.0020	310, 629, above 750
TR + 1% Au *	0.190	0.0020	308, 625, above 750

* Samples were calcined at 150 °C for 3 h.

2.2. CWAO of Glyphosate

The CWAO operating and reaction conditions were chosen based on the results of preliminary experiments, where we used 500 mg of inert SiC and different experimental conditions, such as different reaction temperatures (120 to 180 °C) and different flow rates of the 10.0 mg/L glyphosate aqueous solution (0.5–1 mL/min). The data presented in Figure S10 suggest that, under conditions of 180 °C and a flow rate of 1 mL/min, approximately 75% of the glyphosate undergoes degradation through non-catalytic oxidation reactions within the liquid phase. The rate of glyphosate degradation decreases to about 35, 10 and 5% when the reaction temperature decreases to 150, 135 and 120 °C, respectively. Decreasing the rate of aqueous glyphosate solution from 1 mL/min to 0.5 mL/min at 120 °C exhibits only a minimal effect on the glyphosate degradation rate. Based on these results, we decided to start the CWAO experiment using the synthesized catalysts at 135 °C and a flow rate of 1 mL/min and operate at these conditions for 48 h. After this, we increased the temperature to 150 °C and continued with the experiment for another 48 h.

Figure 5 shows the results of glyphosate and TOC conversions over time in a three-phase trickle-bed reactor packed with the synthesized catalysts. The data were used to calculate glyphosate degradation and TOC conversion over the 96-h CWAO experiment and are listed in Table 3. We also performed CHNS elemental analysis of fresh and 96-h operated catalysts to calculate TOC accumulation (TOC_{accu}) and TOC mineralization (TOC_{miner}, Table 3). After 35 h at 135 °C, all materials achieved steady-state performance. After 48 h, both TiO_2 supports had similar glyphosate degradation rates. The TR support started at nearly 100% degradation, dropping to ~25% in 30 h, while the TP support started at 30% and remained constant. These differences are due to varying S_{BET} values and the nature of acidic surface sites. The TP support's strong acidic sites and lower surface area led to lower initial activity as glyphosate degradation products blocked its surface. The TR support showed slow deactivation over time due to higher initial activity. CHNS analysis (Table 3) confirmed higher TOC_{accu} on the TR support, almost twice that of the TP support, due to its high initial catalytic activity generating more degradation products.

Table 3. Glyphosate conversions obtained in the presence of the investigated catalysts during the whole 96 h on stream. The carbon content, as determined by CHNS elemental analysis, was assessed on the surfaces of newly prepared solids (TC_{fresh}) and catalysts employed in the CWAO process (TC_{spent}). Additionally, the total organic carbon (TOC) conversions (96 h on stream) were correlated with the percentage of TOC deposition observed on the catalyst surfaces (TOC accumulation on the surface of spent catalyst (TOC_{accu}) and TOC mineralization to CO_2 and H_2O (TOC_{miner})).

Sample	Glyphosate Conversion	TOC Conversion	TC_{fresh}	TC_{spent}	TOC_{accu}	TOC_{miner}
	0–96 h	0–96 h				
	%		mg/g		%	
TP	35	19	0.16	0.27	2.7	16.3
TP + 0.5% Au	51	41	0.13	0.46	8.1	33.9
TP + 1% Au	67	48	0.11	0.36	6.1	41.9
TP + 2% Au	45	30	0.17	0.50	8.1	21.9
TR	51	29	0.13	0.33	4.9	24.1
TR + 1% Au	65	42	0.15	0.57	10.3	31.7

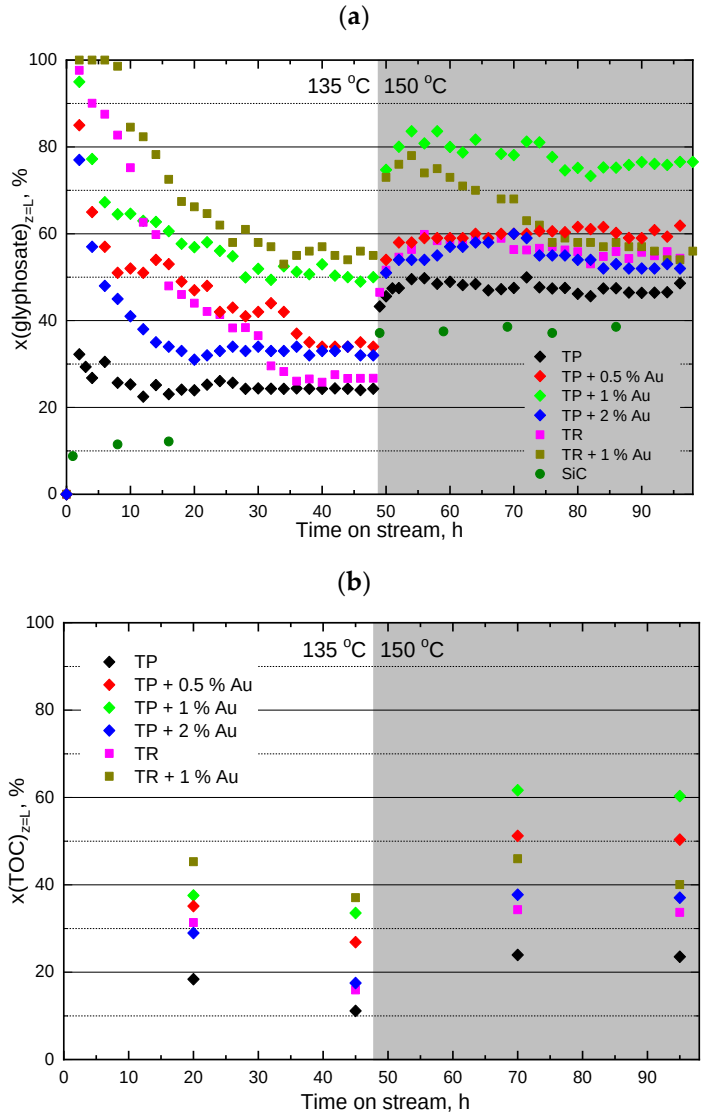

Figure 5. (**a**) Glyphosate and (**b**) TOC conversion as a function of time on the stream obtained in the trickle-bed reactor in the presence of prepared materials.

The results in Figure 5 show that materials containing Au exhibit higher catalytic activity than the bare TiO_2 supports. Heating the catalysts in the CWAO process generates charge carriers, similar to those produced in heterogeneous photocatalysis, by illuminating the catalysts with light of suitable energy [57]. As noted, charge carriers and reactive oxygen species oxidize glyphosate even with only bare TiO_2 supports (Figure 5). Adding Au enhances the separation of electron-hole pairs, reducing signal intensities in the photoluminescence (PL) spectra of TiO_2+Au catalysts compared to bare TiO_2 (Figure S7). UV–Vis DR measurements (Figure S6) suggest that metallic Au in TiO_2+Au catalysts can absorb visible light and near-infrared radiation. It can be tentatively proposed that, in the CWAO process, near-infrared radiation absorbed by Au particles may trigger the Au surface plasmon resonance effect, forming electrons that are injected into the TiO_2 support, thus increasing the catalytic activity of TiO_2+Au catalysts compared to bare TiO_2. For the investigated materials, the surface area of the TiO_2 supports in the TiO_2+Au catalysts is significantly larger than that of the Au particles, which leads to the conclusion that the activation of oxygen in the CWAO process mainly occurs at the surface of the TiO_2 supports. This means that the interface between TiO_2 and Au as well as the surface of Au particles should not be covered by the glyphosate degradation products, so that the Au–TiO_2 junction and the Au particles can participate in the separation and generation of the

charge carriers. We see (Figure 5) that the adsorption of glyphosate degradation products influences the glyphosate degradation rates of the used TiO_2+Au catalysts regardless of which TiO_2 support was used. At 48 h, the highest degradation of glyphosate, when considering only the TP based materials, was achieved by that with 1 wt.% Au loading (~50%) and the lowest by that with 2 wt.% of Au (~35%). The TR + 1% Au catalyst exhibited a 5% higher glyphosate degradation rate after 48 h relative to the TP + 1% Au sample. After increasing the temperature to 150 °C, the glyphosate degradation rates also increased for all tested catalysts by ~15 to 20%, as glyphosate degradation over SiC also increased by ~15%. It should be noted that the desorption of some weakly bound glyphosate degradation products from the catalyst surface can also be achieved by increasing the reaction temperature. Almost all investigated catalysts, except the TR + 1% Au sample, reached a steady-state performance after 10 h on stream at 150 °C. After 48 h at 150 °C (all together 96 h), the highest glyphosate degradation rate was obtained in the presence of TP + 1% Au catalyst (~75%), followed by the TP + 0.5% Au (~62%) and TP + 2% Au (~52%) catalysts. Bare TR support and TR + 1% Au catalyst exhibited almost the same glyphosate degradation rates as the TP + 2% Au sample. In the case of the TR + 1% Au sample, we can see that the initial glyphosate degradation rate was around 75%, which then gradually decreased with the time on stream almost linearly until ~55%, where it reached the glyphosate degradation rate of the bare TR sample. The decline in the glyphosate degradation rate observed with the TR + 1% Au catalyst can be attributed to the accumulation of glyphosate degradation products on the material's surface during the CWAO process. Additionally, the TR + 1% Au catalyst generated a greater quantity of glyphosate degradation products compared to the pristine TR support, further contributing to this effect. Another possibility would be that the Au particles are washed off the TR surface during the CWAO process. For this reason, we also performed SEM–EDX analysis of the spent TiO_2+Au catalysts and, as the results in Table S1 show, the Au loading of the spent catalysts was almost the same as that of the fresh samples. It should be also emphasized that the TR + 1% Au catalyst exhibited the highest carbon accumulation (and highest TOC_{accu}) rate among all the materials investigated, as shown by the CHNS elemental analysis results provided in Table 3. We also measured the TOC conversions at 20, 45, 70 and 95 h on stream. The results displayed in Figure 5b show that the TOC conversion rate orders for the investigated catalysts at 45 and 95 h on stream are the same as the orders for the catalysts based on the glyphosate degradation rates obtained after 48 and 96 h on stream. Furthermore, regarding the TOC conversion rates, an enhancement in conversions is observed for all tested materials with the elevation of the reaction temperature to 150 °C. A comparison of the activity of the catalysts of the TP+Au series shows that a higher Au loading with the same average Au particle size and the same SB height is favourable for the long-term catalytic activity in the CWAO degradation of glyphosate, as the comparison of the samples TP + 0.5% Au and TP + 1% Au shows. This could be due to the fact that the glyphosate degradation products can cover the surface of the Au particles, which represent the catalytically active phase in the CWAO process, more quickly in the case of the 0.5 wt.% Au loading. It can also be said that a higher SB is advantageous, as the TP + 1% Au catalyst already has a higher catalytic activity at the beginning of the CWAO of glyphosate than the TP + 2% Au solid. A higher SB allows the charge carriers to remain in the TiO_2 conduction band and increase their reduction potential [54] for the generation of reactive oxygen species (ROS) as, for example, hydroxyl radicals ($^{\bullet}OH$) and superoxide anion radicals ($^{\bullet}O_2^-$). The presence of the latter in our investigated reactor system is evidenced by the detected degradation products of glyphosate (see Section 3.3), although we cannot clearly state whether they are formed by a direct or indirect process [58]. The low catalytic activity of the TP + 2% Au sample in the CWAO of glyphosate can also stem from the existence of strong acidic sites and glyphosate degradation products adsorption (high TOC_{accu} of 8.1%) [28]. When comparing the performance of TR + 1% Au (TOC_{accu} = 10.3%; TOC_{miner} = 31.7%) and TP + 1% Au (TOC_{accu} = 6.1%; TOC_{miner} = 41.9%) catalysts, it can also be said that a higher SB is favourable for the

catalytic activity in the long-term CWAO run, but it must be taken into account here that smaller Au nanoparticles (d_{Au} = 9.2 nm, Table 1) are found on the TR + 1% Au surface, compared to the TP + 1% Au solid (d_{Au} = 36.9 nm, Table 1), which could be more easily covered with glyphosate degradation products, leading to the catalyst deactivation. In addition, the pyridine TPD profile of TR + 1% Au catalyst (Figure 4) shows the desorption of pyridine even in the temperature range above 750 °C and thus the presence of strong acidic sites that favour the adsorption of carbonaceous deposits during CWAO of glyphosate [28].

TPO analysis of the spent catalysts (results are shown in Figure 6) was employed to monitor the oxidation of the carbonaceous species adsorbed on the surface of the investigated catalyst. Comparing only the TiO_2 supports, the highest weight loss was measured for the TR support, confirming that a larger specific surface area favourably affects the adsorption of glyphosate degradation products, as the calculated weight loss per surface area is almost the same for TR and TP supports (0.0171% weight loss/(m^2/g) for TR and 0.0178% weight loss/(m^2/g) for TP). Further, the TiO_2+Au catalysts exhibited a higher weight loss compared to the bare TiO_2 supports as they also degraded more glyphosate and produced more degradation products. The highest weight loss was measured for the TR + 1% Au catalyst, which is to be expected considering the results of the CWAO runs (and the pyridine TPD and CHNS elemental analyses), where the catalyst showed a high affinity to adsorb glyphosate degradation products. Figure 6b shows the derivations of the mass as a function of temperature for the thermogravimetric measurements. According to the literature research, the peaks up to 410 °C belong to amorphous carbon, those between 410 and 520 °C to single-walled carbon nanotubes and the peaks between 700 and 800 °C to graphite [59]. In the materials we examined, most of the deposits belong to amorphous carbon. However, some products in the form of carbon nanotubes and graphite can also be observed. The latter in particular are known to have a strong adsorption affinity for organic compounds and can thus enhance the apparent removal of glyphosate degradation products from the liquid phase on the catalyst surface [60].

(**a**)

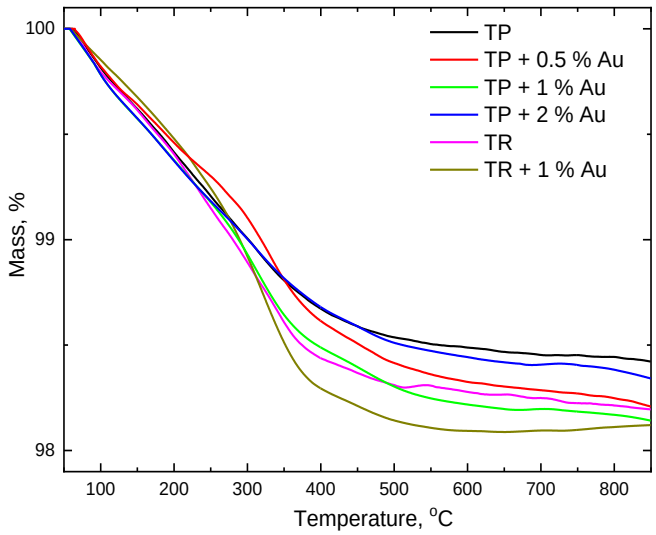

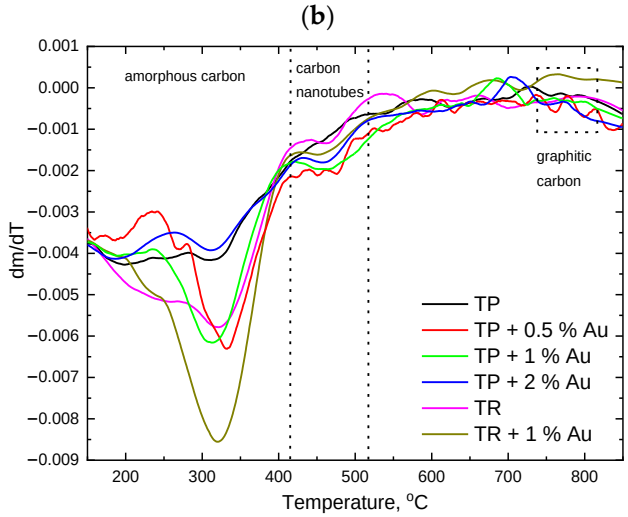

Figure 6. (**a**) TGA–TPO profiles of the TiO_2 and TiO_2+Au samples after use in the CWAO process. (**b**) Derivation of mass as a function of temperature.

2.3. Identification of Degradation Products

One of the goals of our study was also to identify the major degradation products generated during CWAO of glyphosate and, based on the data, propose a possible oxidation pathway characteristic of our reaction system. Multiple investigations posit two conceivable oxidation pathways for glyphosate under oxidative conditions [22,27,61–63]. The initial pathway involves glyphosate transforming into amino-methyl-phosphonic acid (AMPA) through the rupture of the C–N bond. Subsequently, AMPA can undergo further oxidation to yield methylamine, NH_4^+, CH_2O, NO_3^-, and PO_4^{3-}. In an alternative route, glyphosate is transformed into sarcosine via direct cleavage of the C–P bond, which can then be further oxidized to glycine, CH_2O, and NH_4^+. Xing et al. [27], based on their experimental findings regarding the evolution of primary intermediates and end products, proposed a preliminary degradation pathway for glyphosate in the CWAO process utilizing activated carbons as catalysts. Initially, the C–N bond cleavage of glyphosate takes place, yielding equivalent amounts of formaldehyde (CH_2O) and AMPA through reactive radicals as, for example, superoxide anion radicals ($^{\bullet}O_2^-$) and hydroxyl radicals ($^{\bullet}OH$). Subsequently, in the second step, cleavage of the C–N bond of AMPA ensues, leading to the formation of PO_4^{3-}, NH_4^+, and CH_2O. In addition, oxidation of CH_2O and NH_4^+ to HCOOH and NO_3^- takes place. Our qualitative and quantitative data on the catalytic degradation products of glyphosate when using the TP + 1% Au as a model catalyst are shown in Table 4. At t = 0, no degradation products of glyphosate, apart from AMPA, were found in the sample. The unexpected presence of this acid could be explained by a chemical impurity of the commercial glyphosate or by a spontaneous degradation of glyphosate in the aqueous solution, prior to its introduction to the reactor. More importantly, the results in Table 4 demonstrate that the oxidation of glyphosate must include the cleavage of the C–N bond, as both glyoxylic acid and AMPA were detected in samples withdrawn from the reactor after 20–90 h on stream. No traces of sarcosine were found in the tested samples; however, glycine, a downstream degradation product of sarcosine, was determined at similar concentration levels as glyoxylic acid, which indicates that glyphosate also degraded by following a secondary pathway that involves the C–P bond cleavage. Munner et al. [64] observed the same phenomenon, namely that no sarcosine was formed when $^{\bullet}OH$ radicals attacked the non-adsorbed glyphosate, leading to the rupture of the C–P bond and formation of glycine. Other downstream degradation products, such as oxalic acid and MPA, were not detected in the studied samples.

Table 4. Determination of the degradation products of glyphosate in the end-product solutions using the TP + 1% Au catalyst in the CWAO experiment.

Time on Stream	Glyoxylic Acid	Sarcosine	Glycine	Oxalic Acid	MPA	AMPA
h	mg/L					
0	n.d.	n.d.	n.d.	n.d.	n.d.	0.73
20	0.21	n.d.	0.18	n.d.	n.d.	1.20
40	0.25	n.d.	0.32	n.d.	n.d.	1.69
90	0.31	n.d.	0.50	n.d.	n.d.	2.30

n.d.—not detected.

3. Experimental

3.1. Catalyst Preparation

Two distinct TiO_2 substrates underwent wet impregnation to yield TiO_2+Au catalysts. The first, commercially sourced TiO_2 DT-51 (generously provided by CristalACTiV™, Thann, France), designated as TP, underwent a pre-calcination step in air for 2 h at 200 °C before the wet impregnation synthesis process. This pre-treatment ensured that the intrinsic properties of TP remained unaffected by the subsequent operating conditions of the CWAO experiment. TiO_2 nanorods (TR), prepared by a hydrothermal process [65] and using DT-51 as the starting material, were employed as the second TiO_2 support. TR underwent further calcination in air for 2 h at 500 °C to achieve complete transformation of the amorphous TiO_2 to anatase TiO_2. An amount of 0.5 g of the TiO_2 support was added to an aqueous solution of $HAuCl_4 \times 3H_2O$ (25 mL) and stirred for 20 h. The molarity of $HAuCl_4 \times 3H_2O$ was adjusted to obtain TiO_2+Au catalysts with Au weight percent (wt.%) between 0.5 and 2. The suspension was allowed to dry for 12 h at room temperature before undergoing calcination at 300 °C for 2 h, with a heating ramp of 300 °C per hour. The samples were designated as TP(TR) + x% Au, where x indicates the nominal weight percent of Au (from 0.5 to 2).

3.2. Catalyst Characterization

Images of the catalysts' morphology and elemental composition were obtained using a field emission scanning electron microscope (SEM, Carl Zeiss SUPRA 35 VP Oberkochen, Germany) equipped with an energy dispersive X-ray detector spectrometer (EDS) Inca 400 from Oxford Instruments. Additionally, transmission electron microscopy (TEM) analysis was performed using a JEM-2100 instrument from Jeol Inc. (Tokyo, Japan), operating at 200 keV, to generate gold particle size distribution diagrams for the materials under investigation.

The phase composition of the materials under investigation was determined using X-ray powder diffractometry (XRD) with a PANalytical X'pert PRO MPD instrument (Almero, The Netherlands), employing Cu Kα1 radiation (wavelength of 1.54056 Å) in a reflection geometry covering an angular range from 10 to 90° with steps of 0.0341°. Crystalline phases were identified using PDF standards from the International Centre for Diffraction Data (ICDD). Prior to N_2 adsorption–desorption isotherm measurements at −196 °C using the Micromeritics TriStar II 3020 analyzer, the materials underwent pretreatment in an N_2 stream (purity 6.0, Linde, Munich, Germany,) for 1 h at 90 °C and for 4 h at 180 °C using the Micromeritics SmartPrep degasser.

A Perkin Elmer Lambda 650 UV–Vis spectrophotometer equipped with a Harrick (New York, NY, USA) Scientific Praying Mantis DRP-SAP accessory was used to obtain the UV–Vis diffuse reflectance (UV–Vis DR) spectra of the catalysts.

The LS-55 UV–Vis fluorescence spectrometer from Perkin Elmer (Waltham, MA, USA), was used to obtain the photoluminescence (PL) emission spectra of the analyzed materials (excitation wavelength 315 nm).

The valence band maxima (VBM) of the analyzed catalysts were determined using the PHI–TFA XPS spectrometer (Physical Electronics Inc., Chanhassen, MN, USA). The surface of the analyzed materials was excited with X-rays emitted from a monochromatic Al-Kα source with an energy of 1468.6 eV. An energy analyzer with a pass energy of 29 eV and a resolution of 0.6 eV was used to obtain high energy resolution spectra.

The acidic properties of the studied catalysts were measured using the Perkin Elmer Pyris 1 TGA instrument. The studied catalysts were heated for 10 min at 200 °C in air and then cooled to 120 °C. After reaching 120 °C, a stream of N_2 and pyridine was turned on and the catalyst surface was saturated with pyridine for 10 min. To remove the excess pyridine from the catalyst surface, the solids were purged with N_2 for another 90 min. Then, temperature-programmed desorption (TPD) of pyridine was performed by increasing the temperature to 750 °C with a heating ramp of 20 °C/min.

The CHNS elemental analyzer employing the Perkin Elmer 2400 series II was used to determine the extent of carbonaceous deposits on the catalyst surfaces after the CWAO experiments.

The nature of the carbonaceous species accumulated on the surface of the studied catalysts after their use in the CWAO process was determined by the TGA measurements performed with the Perkin Elmer Pyris 1 TGA instrument. The spent catalyst samples were heated from 50 to 850 °C in air (10 °C/min).

A thermogravimetric analysis (TGA-TPO) of the spent catalysts in air (50 mL/min) was performed with the Perkin Elmer Pyris 1 TGA instrument, which allowed us to monitor the oxidation of the carbonaceous species adsorbed on the catalyst surface during the oxidation of the aqueous glyphosate solution.

3.3. Glyphosate Oxidation Runs in a Trickle-Bed Reactor

A computer-controlled and fully automated Microactivity-Reference (MA-Ref) reactor system from PID Eng and Tech (Madrid, Spain) was used to perform the CWAO experiments. The MA-Ref unit can be defined as a continuous-flow, three-phase trickle-bed reactor with the concurrent down-flow of gas and liquid phase. Oxidation of the contaminant dissolved in water was carried out in a Hastelloy C-276 tubular reactor (Autoclave Engineers, Erie, PA, USA) with a length of 305 mm and inner diameter of 9 mm. The tubular reactor was located in the central part of the reactor unit. An HPLC positive alternative displacement pump (Gilson, Middleton, WI, USA, model 307) was used to pump the 10.0 mg/L aqueous glyphosate solution into the reactor unit. The Bronkhorst EL-FLOW HI-TECH mass flow controller was used to supply pure O_2 (Messer, Ruše, Slovenia, USA, purity 5.0) to the reactor system at a prescribed flow rate. Before entering the reactor, the preheated gas and liquid streams were combined in a T-joint. Sintered stainless steel (SS 316, 10 μm) filters were installed at the bottom and top of the reactor to protect the reactor assembly from contamination. A total of 300 mg of a catalyst was placed on a sintered 2 μm frit located in the center of the reactor tube. The reaction temperature was monitored with a K-type thermocouple installed through the top of the reactor tube and in contact with the catalyst bed. The PID temperature controller (TOHO, Sagamihara-Shi, Japan, model TTM-005) was used to control the reaction temperature within ±1.0 °C. The liquid and gas phases were separated at the outlet of the reactor unit using a high-pressure liquid-gas separator cooled by a Peltier cell. The operating conditions for the CWAO experiments are listed in Table 5.

Table 5. The operational parameters of the continuous-flow, three-phase trickle-bed reactor during the CWAO experiments.

Parameter	Value
Mass of catalyst in bed, g	0.3
Reaction temperature, °C	135–150
Total operating pressure, bar	13.1–14.7
Oxygen partial pressure, bar	10.0
Gas flow rate, mL/min	60.0
Liquid flow rate, mL/min	1.0
Glyphosate feed concentration, mg/L	10.0

3.4. Analysis of the End-Product Solutions

Ion chromatography (IC) with pulsed amperometric detection was used to measure glyphosate concentration in liquid-phase samples collected during the CWAO experiments. Measurements were conducted using an Metrohm IC system consisting of a 930 Compact IC Flex with an amperometric detector with working electrode made of gold (3 mm diameter) and reference electrode made of palladium. The working temperature of the amperometric detector was 35 °C. Samples (100 μL) were injected automatically using an 858 Professional Sample Processor. Glyphosate was separated at 30 °C on the Metrosep Carb 2–150/4.0 high-capacity anion separation column. The sodium acetate eluent contained 300 mmol/L sodium acetate and10 mmol/L sodium hydroxide. The eluent flow rate was 0.4 mL/min from 0 to 16 min and 0.8 mL/min from 16 to 30 min. The IC system was controlled by MagIC Net Compact software (version 3.2).

A Shimadzu TOC-L analyzer, paired with an ASI-L autosampler, was employed for the analysis of total organic carbon (TOC) levels in both untreated and treated glyphosate solutions. High-temperature catalytic oxidation of the organics contained in the injected samples was carried out at 680 °C in synthetic air (Messer, purity 5.0). The amount of CO_2 formed was quantified using a calibrated NDIR detector. The observed error for three replicates was within ±1%.

The main intermediates and final products of the glyphosate degradation were identified and quantified by hydrophilic interaction liquid chromatography (HILIC). Chromatographic analyses were carried out on a Thermo Scientific Accela 1250 UHPLC system (Waltham, MA, USA), which was coupled to a Thermo Scientific LTQ Velos mass spectrometer (MS). The separation of compounds was achieved by using a Waters Acquity UPLC BEH HILIC 1.7 μm column (100 × 2.1 mm i.d., Milford, MA, USA). The autosampler and column oven were kept at temperatures of 25 °C and 40 °C, respectively, throughout the experiment. The mobile phase comprised solvent A (40 mM ammonium acetate) and solvent B (10 mM ammonium acetate in a water-acetonitrile mixture at a ratio of 1:9, *v*/*v*). A solvent gradient was employed at a flow rate of 0.6 mL/min as follows: from 0 to 6 min (100% to 60% B), from 6 to 7 min (60% to 100% B), and from 7 to 13 min (maintaining 100% B). The data were acquired by using a PDA detector at 220 nm and by a mass spectrometer scanning in the range m/z = 60–300. Electrospray probe was operated in negative ion mode and the MS parameters were set as follows: spray voltage = 3 kV, T heater = 400 °C, T transfer capillary = 300 °C, sheath gas flow rate = 70 arbitrary units, and auxiliary gas flow rate = 20 arbitrary units. For each analysis, 10 μL of sample was injected, which was prepared in the following manner: the solvent from the aqueous solutions collected from the reactor (1.5 mL) at predetermined time intervals was removed under reduced pressure and the solid residue was reconstituted in 0.15 mL water-acetonitrile (3:7, *v*/*v*) which contained 1 mM EDTA. The resulting solution was then subjected to LC–UV–MS analysis. The samples were analyzed in duplicates. Quantitation of seven analytes, i.e., glyoxylic acid, sarcosine, glycine, oxalic acid, methyl-phosphonic acid (MPA), glyphosate, and amino-methyl-phosphonic acid (AMPA), was carried out by using an external standard calibration method.

4. Conclusions

The objective of this study was to use TiO_2+Au catalysts and CWAO for the degradation of the herbicide glyphosate and to examine the impact of Au loading and the structural characteristics of the anatase TiO_2 supports (nanoparticles (TP, S_{BET} = 88 m^2/g) and nanorods (TR, S_{BET} = 105 m^2/g)) on the catalytic activity of the TiO_2+Au catalysts. The results show that the addition of Au has a positive effect on the glyphosate degradation rate independent of the TiO_2 support and the amount of Au added and that, at the beginning of the CWAO experiment (reaction temperature 135 °C), the TR + 1% Au sample with the largest specific surface area and the lowest SB height has the highest activity. In the TP+Au series, where different Au loadings from 0.5 to 2 wt.% were investigated, the highest catalytic activity was observed for the TP + 1% Au catalyst, which had a higher SB, helping the charge carriers in the TiO_2 conduction band to increase their reduction potential by preventing them from returning to the Au particles. Compared to the TP + 0.5% Au sample, the higher Au loading in the case of the TP + 1% Au catalyst and the presence of more Au particles improved the catalytic activity, as the adsorption and blocking of Au particles by glyphosate degradation products is less detrimental. The detrimental effects of the adsorption of glyphosate degradation products on the catalytic activity of the TiO_2+Au catalysts studied became particularly evident when we increased the reaction temperature to 150 °C. The higher specific surface area of the TR + 1% Au sample and the presence of highly acidic sites favouring the adsorption of glyphosate degradation products, together with the smallest average size of Au particles under the examined TiO_2+Au catalysts, led to an almost linear decrease of the catalytic activity of the TR + 1% Au sample with time on stream. The main degradation products of glyphosate were glyoxylic acid and AMPA, indicating that the glyphosate C–N bond was ruptured. No traces of sarcosine were found, but glycine was determined in similar concentrations as glyoxylic acid, indicating that the glyphosate C–P bond was also cleaved. The results of the present study indicate that high long-term catalytic activity of TiO_2+Au catalysts in the CWAO process for the degradation of glyphosate dissolved in water is a combination of the appropriate specific surface area, SB height, acidic-basic properties, Au loading, and average Au particle size, as obtained in the case of the TP + 1% Au catalyst.

Supplementary Materials: The following supporting information can be downloaded at: https://www.mdpi.com/article/10.3390/catal14070448/s1, Table S1: The outcomes of the SEM-EDS elemental analysis were derived from scans conducted at 15 kV in area scan mode across more than ten randomly chosen locations.; Figure S1. (a) N_2 adsorption-desorption isotherms of the fabricated materials and (b) corresponding BJH pore size distributions.; Figure S2. SEM images of the TiO_2+Au catalysts under investigation are provided alongside corresponding elemental mapping. In these images, the colors cyan, green, and red are used to denote the elemental components of Ti, O, and Au, respectively.; Figure S3. TEM images of the investigated TiO_2+Au catalysts, taken at different magnifications. The red arrows mark the Au nanoparticles detected by TEM elemental analysis.; Figure S4. Au particle size distribution in the investigated TiO_2+Au catalysts.; Figure S5. Zeta potential as a function of pH value for TP and TR supports.; Figure S6. UV-Vis DR spectra of the analyzed TiO_2 supports and TiO_2+Au catalysts.; Figure S7. The photoluminescence (PL) emission spectra in solid-state were captured for both pure TiO_2 supports and the synthesized TiO_2+Au catalysts.; Figure S8. High resolution spectra for (a) O 1s, (b) Ti 2p and (c) Au 4f for the examined catalysts.; Figure S9. TPD of pyridine from the surface of (a) fresh TP and TP + 1 % Au solids and TP and TP + 1 % Au samples calcined at 150 °C for 3 h in air (marked as TP calc@150°C/3 h and TP + 1% Au calc@150°C/3 h), and (b) fresh TR and TR + 1 % Au solids and TR and TR + 1 % Au samples calcined at 150 °C for 3 h in air (marked as TR calc@150 °C/3 h and TR + 1% Au calc@150°C/3 h).; Figure S10. Conversion of glyphosate as a function of temperature and flow rate obtained in the trickle-bed reactor in the presence of 500 mg SiC ($c_{glyphosate,\ feed}$ = 10.0 mg/L).

Author Contributions: Conceptualization, G.Ž. and A.P.; methodology, G.Ž and A.A.; validation, G.Ž. and A.P.; formal analysis, G.Ž. and A.A.; investigation, G.Ž. and A.A.; resources, A.A. and A.P.; writing—original draft preparation, G.Ž. and A.A.; writing—review and editing, G.Ž., A.A. and A.P.; visualization, G.Ž. and A.A.; supervision, G.Ž.; funding acquisition, A.A. and A.P. All authors have read and agreed to the published version of the manuscript.

Funding: The authors acknowledge financial support from the Slovenian Research and Innovation Agency (research core funding nos. P2-0150 and P1-0005).

Data Availability Statement: Data will be made available on request.

Acknowledgments: The authors thank Janez Zavašnik and Janez Kovač (Jožef Stefan Institute, Ljubljana, Slovenia) for carrying out TEM and XPS analyses.

Conflicts of Interest: The authors declare that they have no known competing financial interests or personal relationships that could have appeared to influence the work reported in this paper.

References

1. Roy, S.; Vashishtha, M.; Saroha, A.K. Catalytic wet air oxidation of oxalic acid using platinum catalyst in bubble column reactor. *J. Eng. Sci. Tech. Rev.* **2010**, *3*, 95–107.
2. Luck, F. Wet air oxidation: Past, present and future. *Catal. Today* **1999**, *53*, 81–91.
3. Levec, J.; Pintar, A. Catalytic wet-air oxidation processes: A review. *Catal. Today* **2007**, *124*, 172–184.
4. Cybulski, A. Catalytic wet air oxidation: are monolithic catalysts and reactors feasible? *Ind. Eng. Chem. Res.* **2007**, *46*, 4007–4033.
5. Bistan, M.; Tišler, T.; Pintar, A. Catalytic and photocatalytic oxidation of aqueous bisphenol a solutions: Removal, toxicity, and estrogenicity. *Ind. Eng. Chem. Res.* **2011**, *51*, 8826–8834.
6. Pintar, A.; Batista, J.; Tišler, T. Catalytic wet-air oxidation of aqueous solutions of formic acid, acetic acid and phenol in a continuous-flow trickle-bed reactor over Ru/TiO_2 catalysts. *Appl. Catal. B* **2008**, *84*, 30–41.
7. Erjavec, B.; Kaplan, R.; Djinović, P.; Pintar, A. Catalytic wet air oxidation of bisphenol A model solution in a trickle-bed reactor over titanate nanotube-based catalysts. *Appl. Catal. B* **2013**, *132–133*, 342–352.
8. Kaplan, R.; Erjavec, B.; Senila, M.; Pintar, A. Catalytic wet air oxidation of bisphenol A solution in a batch-recycle trickle-bed reactor over titanate nanotube-based catalysts. *Environ. Sci. Pollut. Res.* **2014**, *21*, 11313–11319.
9. Thongprakaisang, S.; Thiantanawat, A.; Rangkadilok, N.; Suriyo, T.; Satayavivad, J. Glyphosate induces human breast cancer cells growth via estrogen receptors. *Food Chem. Toxicol.* **2013**, *59*, 129–136.
10. Rani, L.; Thapa, K.; Kanojia, N.; Sharma, N.; Singh, S.; Grewal, A.S.; Srivastav, A.L.; Kaushal, J. An extensive review on the consequences of chemical pesticides on human health and environment. *J. Clean. Prod.* **2021**, *283*, 124657.
11. Muñoz, J.P.; Bleak, T.C.; Calaf, G.M. Glyphosate and the key characteristics of an endocrine disruptor: A review. *Chemosphere* **2021**, *270*, 128619.
12. Zhang, J.W.; Xu, D.Q.; Feng, X.Z. The toxic effects and possible mechanisms of glyphosate on mouse oocytes. *Chemosphere* **2019**, *237*, 124435.
13. Kudsk, P.; Mathiassen, S.K. Pesticide regulation in the European Union and the glyphosate controversy. *Weed Sci.* **2020**, *68*, 214–222.
14. Jacquet, F.; Delame, N.; Vita, J.L.; Huyghe, C.; Reboud, X. The microeconomic impacts of a ban on glyphosate and its replacement with mechanical weeding in French vineyards *Crop Prot.* **2021**, *150*, 105778.
15. Matousek, T.; Mitter, H.; Kropf, B.; Schmid, E.; Vogel, S. Farmers' intended weed management after a potential glyphosate Ban in Austria. *Environ. Manag.* **2022**, *69*, 871–886.
16. Leonelli, G.C. The glyphosate saga continues: 'dissenting'member states and the European way forward. *Transl. Environ. Law* **2023**, *12*, 200–224.
17. Peruzzo, P.J.; Porta, A.A.; Ronco, A.E. Levels of glyphosate in surface waters, sediments and soils associated with direct sowing soybean cultivation in north pampasic region of Argentina. *Environ. Pollut.* **2008**, *156*, 61–66.
18. Botta, F.; Lavison, G.; Couturier, G.; Alliot, F.; Moreau-Guigon, E.; Fauchon, N.; Guery, B.; Chevreuil, M.; Blanchoud, H. Transfer of glyphosate and its degradate AMPA to surface waters through urban sewerage systems. *Chemosphere* **2009**, *77*, 133–139.
19. European Community Council. *L330, 32-5498/83 EEC Directive Concerning the Quality of Water Intended for Human Consumption:* Official Journal of the European Communities: Luxembourg, 1998.
20. Muñoz, P.G.; Dachtler, W.; Altmayer, B.; Schulz, R.; Robert, D.; Seitz, F.; Rosenfeldt, R.; Keller, N. Reaction pathways, kinetics and toxicity assessment during the photocatalytic degradation of glyphosate and myclobutanil pesticides: Influence of the aqueous matrix. *Chem. Eng. J.* **2020**, *384*, 123315.
21. El Agrebi, N.; Tosi, S.; Wilmart, O.; Scippo, M.L.; de Graaf, D.C.; Saegerman, C. Honeybee and consumer's exposure and risk characterisation to glyphosate-based herbicide (GBH) and its degradation product (AMPA): Residues in beebread, wax, and honey. *Sci. Total Environ.* **2020**, *704*, 135312.
22. Manassero, A.; Passalia, C.; Negro, A.C.; Cassano, A.E.; Zalazar, C.S. Glyphosate degradation in water employing the H_2O_2/UVC process. *Water Res.* **2010**, *44*, 3875–3882.
23. Bonansea, R.I.; Filippi, I.; Wunderlin, D.A.; Marino, D.J.G.; Amé, M.V. The fate of glyphosate and AMPA in a freshwater endorheic basin: An ecotoxicological risk assessment. *Toxics* **2017**, *6*, 3.
24. Van Bruggen, A.H.C.; He, M.M.; Shin, K.; Mai, V.; Jeong, K.C.; Finckh, M.R.; Morris, J.G., Jr. Environmental and health effects of the herbicide glyphosate. *Sci. Total Environ.* **2018**, *616–617*, 255–268.
25. Gupta, P.; Pandey, K.; Verma, N. Augmented complete mineralization of glyphosate in wastewater via microbial degradation post CWAO over supported Fe-CNF. *J. Chem. Eng.* **2022**, *428*, 132008.

26. Gupta, P.; Verma, N. Evaluation of degradation and mineralization of glyphosate pollutant in wastewater using catalytic wet air oxidation over Fe-dispersed carbon nanofibrous beads. *J. Chem. Eng.* **2021**, *417*, 128029.
27. Xing, B.; Chen, H.; Zhang, X. Efficient degradation of organic phosphorus in glyphosate wastewater by catalytic wet oxidation using modified activated carbon as a catalyst. *Environ. Technol.* **2018**, *39*, 749–758.
28. Žerjav, G.; Kaplan, R.; Pintar, A. Catalytic wet air oxidation of bisphenol A aqueous solution in trickle-bed reactor over single TiO_2 polymorphs and their mixtures. *J. Environ. Chem. Eng.* **2018**, *6*, 2148–2158.
29. Cojocaru, B.; Andrei, V.; Tudorache, M.; Lin, F.; Cadigan, C.; Richards, R.; Parvulescu, V.I. Enhanced photo-degradation of bisphenol pollutants onto gold-modified photocatalysts. *Catal. Today* **2017**, *284*, 153–159.
30. Shi, D.; Liu, J.; Ji, S. Preparation of Au/TiO_2 catalyst and the performance of liquid methanol catalytic oxidation to formic acid. *Ind. Eng. Chem. Res.* **2017**, *56*, 11028–11033.
31. Alvaro, M.; Cojocaru, B.; Ismail, A.A.; Petrea, N.; Ferrer, B.; Harraz, F.A.; Parvulescu, V.I.; Garcia, H. Visible-light photocatalytic activity of gold nanoparticles supported on template-synthesized mesoporous titania for the decontamination of the chemical warfare agent Soman. *Appl. Catal. B* **2010**, *99*, 191–197.
32. Mrowetz, M.; Villa, A.; Prati, L.; Selli, E. Effects of Au nanoparticles on TiO_2 in the photocatalytic degradation of an azo dye. *Gold Bull.* **2007**, *40*, 154–160.
33. Žerjav, G.; Say, Z.; Zavašnik, J.; Finšgar, M.; Langhammer, C.; Pintar, A. Photo, thermal and photothermal activity of TiO_2 supported Pt catalysts for plasmon-driven environmental applications. *J. Environ. Chem. Eng.* **2023**, *11*, 110209.
34. D'Agostino, C.; Brett, G.; Divitini, G.; Ducati, C.; Hutchings, G.J.; Mantle, M.D.; Gladden, L.F. Increased affinity of small gold particles for glycerol oxidation over Au/TiO_2 probed by NMR relaxation methods. *ACS Catal.* **2017**, *7*, 4235–4241.
35. Žerjav, G.; Roškarič, M.; Zavašnik, J.; Kovač, J.; Pintar, A. Effect of Au loading on Schottky barrier height in TiO_2 + Au plasmonic photocatalysts. *Appl. Surf. Sci.* **2022**, *579*, 152196.
36. Huang, X.; El-Sayed, M.A. Gold nanoparticles: Optical properties and implementations in cancer diagnosis and photothermal therapy. *J. Adv. Res.* **2010**, *1*, 13–28.
37. Yu, J.G.; Xiong, J.F.; Cheng, B.; Liu, S.W. Fabrication and characterization of Ag-TiO_2 multiphase nanocomposite thin films with enhanced photocatalytic activity. *Appl. Catal. B* **2005**, *60*, 211–221.
38. Shu, Y.; Ji, J.; Zhou, M.; Liang, S.; Xie, Q.; Li, S.; Liu, B.; Deng, J.; Cao, J.; Liu, S.; Huang, H. Selective photocatalytic oxidation of gaseous ammonia at ppb level over Pt and F modified TiO_2. *Appl. Catal. B* **2022**, *300*, 120688.
39. Jovic, V.; Al-Azri, Z.H.N.; Chen, W.T.; Sun-Waterhouse, D.; Idriss, H.; Waterhouse, G.I.N. Photocatalytic H_2 production from ethanol-water mixtures over Pt/TiO_2 and Au/TiO_2 photocatalysts: A comparative study. *Top. Catal.* **2013**, *56*, 1139–1151.
40. Serpone, N.; Lawless, D.; Khairutdinov, R. Size effects on the photophysical properties of colloidal anatase TiO_2 particles: Size quantization or direct transitions in this indirect semiconductor? *J. Phys. Chem.* **1995**, *99*, 16646–16654.
41. Nakajima, H.; Mori, T.; Watanabe, M. Influence of platinum loading on photoluminescence of TiO_2 powder. *J. Appl. Phys.* **2004**, *96*, 925–927.
42. Nakajima, H.; Mori, T. Photoluminescence of Pt-loaded TiO_2 powder. *Phys. B* **2006**, *376–377*, 820–822.
43. Abazović, N.D.; Čomor, M.I.; Dramićanin, M.D.; Jovanović, D.J.; Ahrenkiel, S.P.; Nedeljković, J.M. Photoluminescence of anatase and rutile TiO_2 particles. *J. Phys. Chem. B* **2006**, *110*, 25366–25370.
44. Kernazhitsky, L.; Shymanovska, V.; Gavrilko, T.; Naumov, V.; Fedorenko, L.; Kshnyakin, V.; Baran, J. Room temperature photoluminescence of anatase and rutile TiO_2 powders. *J. Lumin.* **2014**, *146*, 199–204.
45. Dupin, J.-C.; Gonbeau, D.; Vinatier, P.; Levasseur, A. Systematic XPS studies of metal oxides, hydroxides and peroxides. *Phys. Chem. Chem. Phys.* **2000**, *2*, 1319–1324.
46. Schumacher, B.; Plzak, V.; Cai, J.; Behm, R.J. Reproducibility of highly active Au/TiO_2 catalyst preparation and conditioning. *Catal. Lett.* **2005**, *101*, 215–224.
47. Liu, H.; Yang, W.; Ma, Y.; Cao, Y.; Yao, J.; Zhang, J.; Hu, T. Synthesis and characterization of titania prepared by using a photoassisted sol−gel method. *Langmuir* **2003**, *19*, 3001–3005.
48. Chen, H.; Li, P.; Umezawa, N.; Abe, H.; Ye, J.; Shiraishi, K.; Ohta, A.; Miyazaki, S. Bonding and Electron Energy-Level Alignment at Metal/TiO_2 Interfaces: A Density Functional Theory Study. *J. Phys. Chem. C* **2016**, *120*, 5549–5556.
49. Arshad, M.S.; Trafela, Š.; Rožman, K.Ž.; Kovač, J.; Djinović, P.; Pintar, A. Determination of Schottky barrier height and enhanced photoelectron generation in novel plasmonic immobilized multisegmented (Au/TiO_2) nanorod arrays (NRAs) suitable for solar energy conversion applications. *J. Mater. Chem. C* **2017**, *5*, 10509–10516.
50. Yang, J.H.; Henao, J.D.; Raphulu, M.C.; Wang, Y.; Caputo, T.; Groszek, A.J.; Kung, M.C.; Scurrell, M.S.; Miller, J.T.; Kung, H.H. Activation of Au/TiO_2 Catalyst for CO Oxidation. *J. Phys. Chem. B* **2005**, *109*, 10319–10326.
51. Murdoch, M.; Waterhouse, G.I.N.; Nadeem, M.A.; Metson, J.B.; Keane, M.A.; Howe, R.F.; Llorca, J.; Idriss, H. The effect of gold loading and particle size on photocatalytic hydrogen production from ethanol over Au/TiO_2 nanoparticles. *Nat. Chem.* **2011**, *3*, 489–492.
52. Jovic, V.; Chen, W.-T.; Sun-Waterhouse, D.; Blackford, M.G.; Idriss, H.; Waterhouse, G.I.N. Effect of gold loading and TiO_2 support composition on the activity of Au/TiO_2 photocatalysts for H_2 production from ethanol–water mixtures. *J. Catal.* **2013**, *305*, 307–317.
53. Zhang, Z.; Yates, J.T. Band bending in semiconductors: Chemical and physical consequences at surfaces and interfaces. *Chem. Rev.* **2012**, *112*, 5520–5551.

54. Qian, K.; Sweeny, B.C.; Johnston-Peck, A.C.; Niu, W.; Graham, J.O.; DuChene, J.S.; Qiu, J.; Wang, Y.-C.; Engelhard, M.H.; Su, D.; et al. Surface plasmon-driven water reduction: Gold nanoparticle size matters. *J. Am. Chem. Soc.* **2014**, *136*, 9842–9845.
55. Erjavec, B.; Tišler, T.; Kaplan, R.; Pintar, A. Titanate nanotubes as a novel catalyst for removal of toxicity and estrogenicity of bisphenol A in the CWAO process. *Ind. Eng. Chem. Res.* **2013**, *52*, 12559–12566.
56. Xu, R.; Gao, Z.; Chen, J.; Yan, W. *From Zeolite to Porous MOF Materials*, 1st ed.; Elsevier: Amsterdam, The Netherlands, 2007.
57. Ibhadon, A.O.; Fitzpatrick, P. Heterogeneous Photocatalysis: Recent Advances and Applications. *Catalysts* **2013**, *3*, 189–218.
58. Nosaka, Y.; Nosaka, A.Y. Generation and Detection of Reactive Oxygen Species in Photocatalysis. *Chem. Rev.* **2017**, *117*, 11302–11336.
59. Luxembourg, D.; Flamant, G.; Laplaze, D. Solar synthesis of single-walled carbon nanotubes at medium scale. *Carbon* **2005**, *43*, 2302–2310.
60. Zhang, L.; Cheng, H.; Zong, R.; Zhu, Y. Photocorrosion suppression of ZnO nanoparticles via hybridization with graphite-like carbon and enhanced photocatalytic activity. *J. Phys. Chem. C* **2009**, *113*, 2368–2374.
61. Chen, S.; Liu, Y. Study on the photocatalytic degradation of glyphosate by TiO_2 photocatalyst. *Chemosphere* **2007**, *67*, 1010–1017.
62. Echavia, G.R.M.; Matzusawa, F.; Negishi, N. Photocatalytic degradation of organophosphate and phosphonoglycine pesticides using TiO_2 immobilized on silica gel. *Chemosphere* **2009**, *76*, 595–600.
63. Barrett, K.A.; McBride, M.B. Oxidative degradation of glyphosate and aminomethylphosphonate by manganese oxide. *Environ. Sci. Technol.* **2005**, *39*, 9223–9228.
64. Muneer, M.; Boxall, C. Photocatalyzed degradation of a pesticide derivative glyphosate in aqueous suspensions of titanium dioxide. *Int. J. Photoenergy* **2008**, *2008*, 197346. https://doi.org/10.1155/2008/197346.
65. Žerjav, G.; Arshad, M.S.; Djinović, P.; Zavašnik, J.; Pintar, A. Electron trapping energy states of TiO_2-WO_3 composites and their influence on photocatalytic degradation of bisphenol A. *Appl. Catal. B* **2017**, *209*, 273–284.